



X-ray tomography-assisted study of a phase inversion process in ceramic hollow fiber systems – Towards practical structural design



Tao Li^{a,1}, Xuekun Lu^{b,1}, Bo Wang^a, Zhentao Wu^c, Kang Li^a, Dan J.L. Brett^b, Paul R. Shearing^{b,*}

^a Department of Chemical Engineering, Imperial College London, London SW7 2AZ, UK

^b Electrochemical Innovation Lab, Department of Chemical Engineering, University College London, London WC1E 7JE, UK

^c School of Engineering and Applied Science, Aston University, Birmingham B4 7ET, UK

ARTICLE INFO

Keywords:

X-ray tomography
Ceramic hollow fibers
Micro-channel 3D characterization
Mass transport
Polymer binder effect

ABSTRACT

Phase inversion-assisted extrusion processes provide a feasible approach for the development of micro-structured ceramic hollow fibers. The mass transport of the hollow fiber, which is closely correlated to the pore structure, is especially important in the application of fuel cell electrodes and membrane reactors. Whilst the relationship between the pore microstructure and the fabrication factors has been the subject of significant investigations, there remains much disagreement in the literature. Recent development in X-ray computed tomography (CT) has enabled new insight into 3D microstructures, which could help to realize practical morphology design and optimization. In this study, a series of alumina hollow fibers have been prepared with varied polymer binder (polyethersulfone, PESf) concentration and new polymer-based internal coagulant (aqueous solution of polyvinyl alcohol, PVA). For the first time, the micro-channels were characterized in 3D using X-ray CT to determine micro-channel densities and diameters in the radial direction, as well as the 2D measurement of the pore size in the sponge-like layer. Water permeation tests were then conducted to correlate the micro-structure of the hollow fiber to the permeability. Results show that the diameter of the micro-channels decreases as the concentration of polymer binder increases, but the pore size in the spongy-like layer becomes larger. When the polymer binder concentration is increased from 16 wt% to 30 wt%, the maximum micro-channel diameter is almost halved (from 29 to 15 μm), and the radial length is 60% longer, whereas the mean flow pore size in the sponge-like layer is increased from approximately 288 to 422 nm. Larger pore size in the spongy-like layer of the high PVA concentration sample contributes to a better permeability (pure water flux almost doubled), but the dimension of the micro-channels is less important. This study provides a new approach to optimize fabrication of hollow fibers for various applications.

1. Introduction

Ceramic membranes have generated a considerable amount of research interest in recent decades for diverse applications such as filtration, desalination, gas separation and membrane reactors and as electrodes for tubular solid oxide fuel cells (SOFC) [1]. Compared to polymeric membranes, ceramic membrane systems display many benefits, including excellent thermal and chemical stability, enabling operation at high temperature and pressure, and under corrosive environments. Moreover, improved mechanical robustness enables easy cleaning of membrane modules and subsequently enhanced long-term operation. Among various designs of ceramic membranes, the hollow fiber geometry shows a unique feature of superior surface area to volume ratio, which is typically more than one order of

magnitude higher than planar and monolithic designs [1].

In terms of fabrication techniques, phase inversion-assisted extrusion has drawn an increasing level of attention recently [1–5]. Compared to other fabrication routes, the phase inversion process leads to a unique, asymmetric structure of resultant hollow fiber membranes, which allows them to be not only directly used in many separation processes, but also to serve as a porous support for composite membrane preparation. However, this technique is yet to be applied in large-scale applications due to the deterrent of system complexity: generally, the process includes the immersion of a slurry, (which is mainly composed of ceramic powder, solvent and polymer binder), into a non-solvent bath; such dynamic manufacturing processes involve continuous solvent/non-solvent exchange and polymer binder precipitation. The final morphology depends significantly on a

* Corresponding author.

E-mail address: p.shearing@ucl.ac.uk (P.R. Shearing).

¹ These authors made an equal contribution to the work.

number of factors, such as suspension composition, selection of coagulant and corresponding extrusion rates. The sensitivity of the hollow fiber microstructure to different parameters can lead to poor repeatability between batches. The internal coagulant is critical in determining the lumen shape and membrane morphology, particularly during dry-jet, wet spinning processes. Despite being almost exclusively applied as an internal coagulant, water is more likely to lead to the formation of abnormal structures due to its negligible viscosity, resulting in irregular cross-section shape [6–8], eccentric lumen [9,10] and non-uniform structure throughout the fiber.

The polymer binder is another critical component affecting the hollow fiber properties and its effects have been investigated in previous work [5,7,11]. It has been widely acknowledged that the microstructure of the resultant membrane (porosity, pore size distribution, tortuosity, etc.) and subsequently the mass transport properties (gas/liquid permeability) are strongly dependent on polymer binder selection and concentration in the suspension. In spite of this, the micro-channels have received limited attention, mainly due to the lack of approach providing detailed insight into the actual interaction between the polymer binder and the microstructure of the porous micro-channel region.

Conventionally, microstructural analysis is predominantly based on 2D imaging techniques, such as scanning electron microscopy (SEM) and transmission electron microscopy (TEM). However, these 2-D techniques do not give access to the actual 3D shape and spatial distribution of the microstructure and require significant repetition to obtain statistically relevant results. Recently, focused ion-beam SEM (FIB-SEM) has received significant research attention [12–18] as it enables experimentalists to understand the variation of microstructure in 3D, beneath the sample surface. However, the long data acquisition time restricts the sample volume investigated and moreover, this destructive method makes it impossible for repeated, or time-lapse testing. X-ray computed tomography (CT) is a popular non-destructive technique widely used for 3D visualisation and characterization of materials by back-projecting sequential 2-D projections to form a virtual 3D volume. This technique has been applied to the study of hollow fiber membranes to relate the morphologies of the pores to processing conditions, to explore the mechanisms of the macro-void initiation, and evaluate the effect of solution saturation [13,14,19].

In this paper we develop this methodology and present new geometrical metrics for characterization of micro-channel structures, aiming for (1) understanding the effects of polymer binder concentration on the microstructure of the micro-channels and the “sponge” region in alumina hollow fiber membranes fabricated by a new polymer-based internal coagulant (aqueous solution of polyvinyl alcohol, PVA); (2) correlating the variations of the permeability to the microstructure and assessing the dominating factors affecting mass transport properties.

For the first time, X-ray CT is used to quantify the micro-channel densities and the cross-sectional dimension of the micro-channels along the radial direction. This study can significantly contribute to the knowledge of processing factors determining the macroscopic and microscopic properties of hollow fiber membrane for various applications.

2. Experimental

2.1. Materials

Aluminium oxide powders of 0.35 μm (alpha, 99.85% metals basis, specific surface area 4.5 $\text{m}^2 \text{g}^{-1}$) were purchased from Advanced Materials (USA) and used as supplied. Polyethersulfone (PESf, Radal A300, Ameco Performance, USA), Arlacel P135 (polyethyleneglycol 30-dipolyhydroxystearate, Uniqema) and polyvinyl alcohol (PVA, Approx. M.W. 145000, Merck Schuchardt, Germany) were applied as binder, dispersant and internal coagulant, respectively. N-Methyl-2-pyrrolidone (HPLC grade, VWR International) was used as the solvent.

Table 1

Suspension compositions and fabricating conditions of different alumina hollow fibers.

	Solid loading (%)	Polymer concentration (polymer/solvent)	PVA solution extrusion rates (ml min^{-1})	Suspension extrusion rate (ml min^{-1})	Air gap (cm)
A1	58.1	16 wt%	10	8	2
A2			15		
B1		20 wt%	10		
B2			15		
C1		25 wt%	10		
C2			15		
D1		30 wt%	10		
D2			15		

2.2. Fabrication of alumina hollow fibers

Aluminium oxide powders were first mixed with the solvent and dispersant and milled for 48 h in a planetary ball mill at 260 rpm (SFM-1, MTI Corporation). The milling was further conducted for 48 h after adding in polymer binder to obtain homogeneous suspensions. The suspension was degassed under vacuum to eliminate air bubbles trapped inside before being transferred into stainless steel syringes. Both suspension and PVA aqueous solution (internal coagulant) were extruded through a tube-in-orifice spinneret into an external coagulant bath to form the hollow fiber precursors, during which the extrusion rates of both components were precisely controlled by syringe pumps (Harvard PHD22/200Hpsi). Details of the compositions and fabrication conditions can be found in Table 1. Hollow fiber samples are classified into four groups, denoted from A to D, with corresponding polymer loading ranging from 16 to 30 wt%. Within each group, two different extrusion rates of internal coagulant have been attempted, which are 10 and 15 ml min^{-1} . The precursors were left in the coagulation bath overnight before being straightened and dried. Then, the precursors underwent a sintering process (Carbolite furnace) to form the final ceramic hollow fibers: the temperature was increased to 600 $^{\circ}\text{C}$ at a heating rate of 2 $^{\circ}\text{C min}^{-1}$ and held for 2 h, and then heated to the target temperature of 1500 $^{\circ}\text{C}$ at a rate of 5 $^{\circ}\text{C min}^{-1}$ and held for 4 h, finally the furnace was cooled to room temperature at a rate of 5 $^{\circ}\text{C min}^{-1}$.

2.3. Materials characterization

Prepared materials were characterized using SEM (JEOL JSM-5610 LV). A clean cross section was obtained by snapping the fibers and samples were subsequently placed vertically on a metal holder. Prior to the imaging, samples were sputter coated with gold (EMITECH Model K550). Secondary electron (SE) imaging mode was adopted to obtain images at varying magnifications using an acceleration voltage of 20 kV. The pore size in sponge-like layer is determined by gas–liquid displacement measurements using PoroLux 100 Porometer with commercial wetting liquid (Porefil, surface tension of 16 mN m^{-1}). Three specimens were tested for each type of sample, with standard deviations of pore size less than 5%. Pure water flux was measured using a custom-designed dead-end system: three samples were tested for each type of membrane with an in-out mode and the average value was calculated with standard deviations of less than 10%. Due to the differences in morphology between different samples, the outer diameter of fiber was used to calculate the surface area.

Non-destructive X-ray computed tomography (CT) was performed using a Zeiss Xradia Versa 520 X-ray microscope operated at 80 kV [20]. The source to test-piece distance and test-piece to detector distance are 13 and 30 mm, respectively, a 4X optically coupled objective lens was applied to achieve a resolution of 1.03 μm and a cylindrical imaged volume of 2 \times 2 \times 2 mm^3 . During sample rotation, 2001 projections were collected with 18 s exposure time using a 16-bit

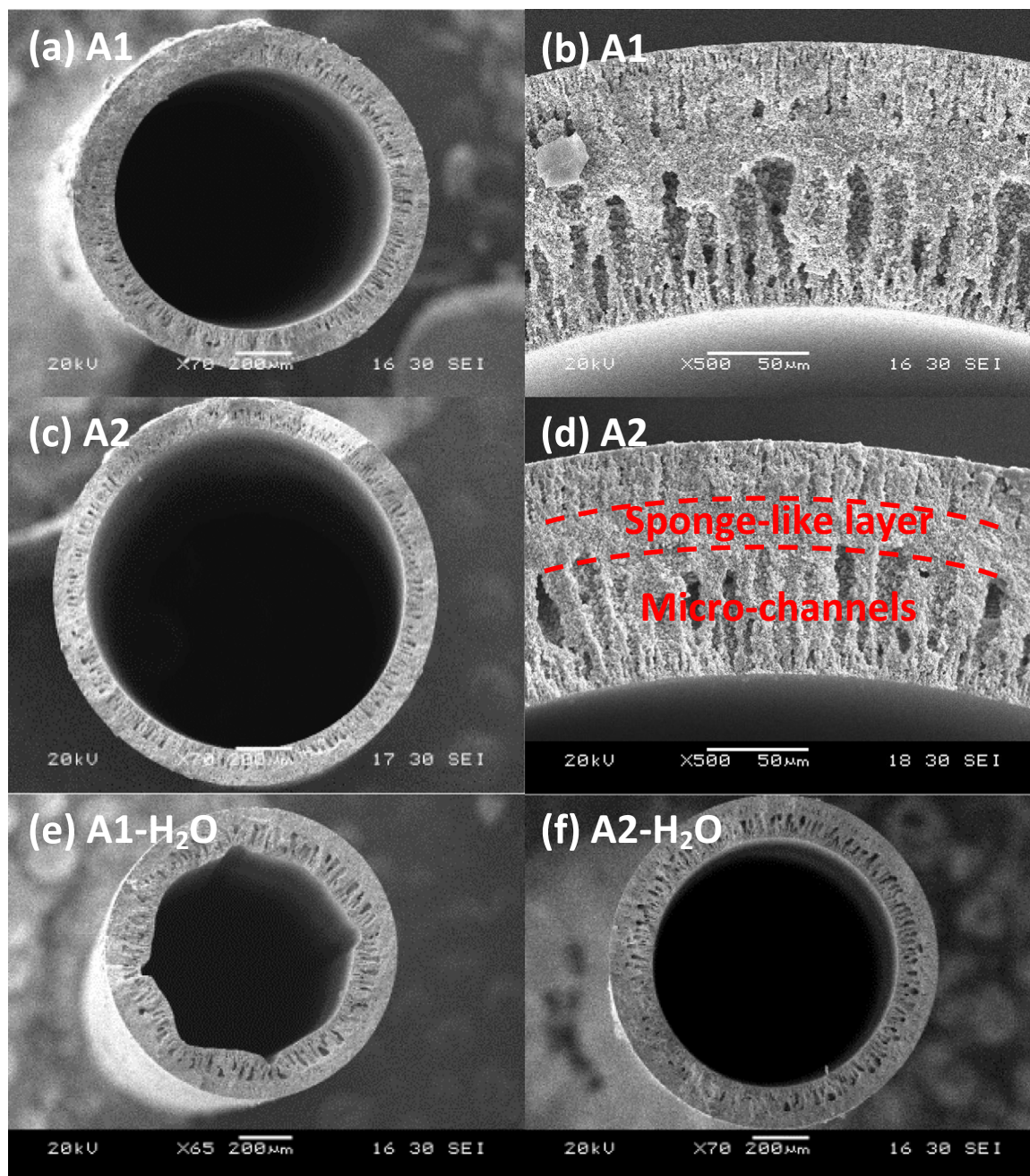


Fig. 1. SEM images of samples with 16 wt% polymer loading, (e) and (f) are the counterparts with water as internal coagulant (water extrusion rates of 10 and 15 ml min⁻¹ for sample A1-H₂O and A2-H₂O, respectively).

2000 by 2000 pixel detector. A filtered-back projection algorithm (Zeiss XMReconstructor) [21,22] was used for the reconstruction and the 3D volume was segmented using gray-scale thresholding method, visualized and characterized using the Avizo V9.0 and Matlab 2014a software packages [23–25].

3. Results

3.1. 2-D morphology and micro-structure

3.1.1. Micro-channels

Fig. 1 shows the SEM images of samples with 16 wt% polymer concentration. As shown in the images, a typical asymmetric structure can be observed in all samples, which is composed of self-organized micro-channels and a sponge-like layer (as shown in Fig. 1(d)). It is

noteworthy that micro-channels from outer surface can also be observed, which were formed due to the phase inversion between the suspension and external water bath with no specific controls over solvent/non-solvent exchange implemented. Therefore, the micro-channels originated from inner surface, which are more ‘responsive’ to internal coagulant adjustment, were investigated in subsequent X-ray CT-assisted study. For example, it can be illustrated that the morphology could be quite significantly affected when water is used as internal coagulant, as shown in Fig. 1(e). Generally, the geometry of the lumen is determined by precipitation rate and the compressive force from the internal coagulant; due to its negligible viscosity compared with the suspension, using water as the internal coagulant normally requires relatively high extrusion rates to provide sufficient force for a regular lumen shape. Such sensitivity over extrusion rate could dramatically restrict the controllability and repeatability of sample

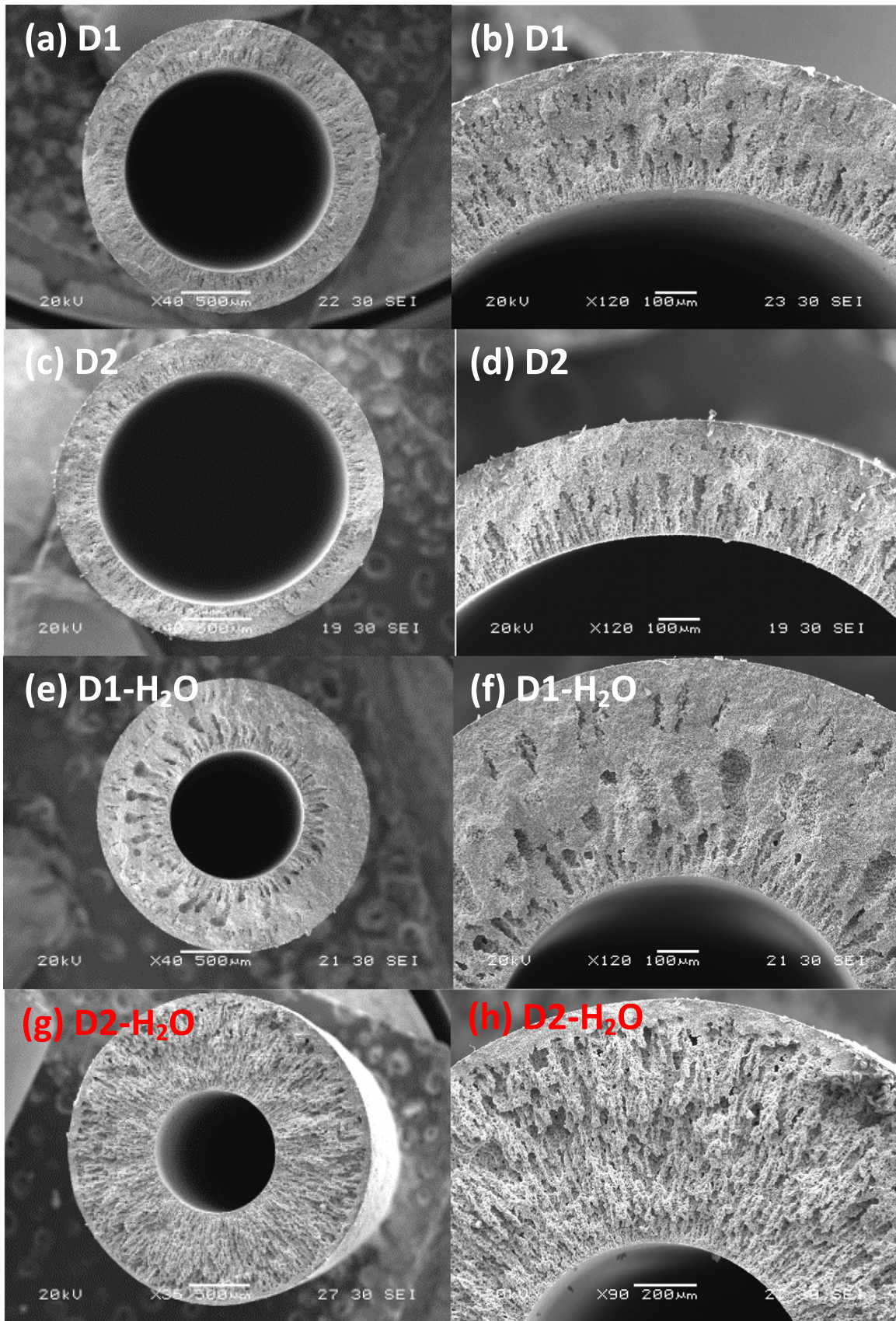


Fig. 2. SEM images of samples with 30 wt% polymer loading, (e) to (h) are the counterparts with water as internal coagulant. Finger-splitting is observed in (g) and (h).

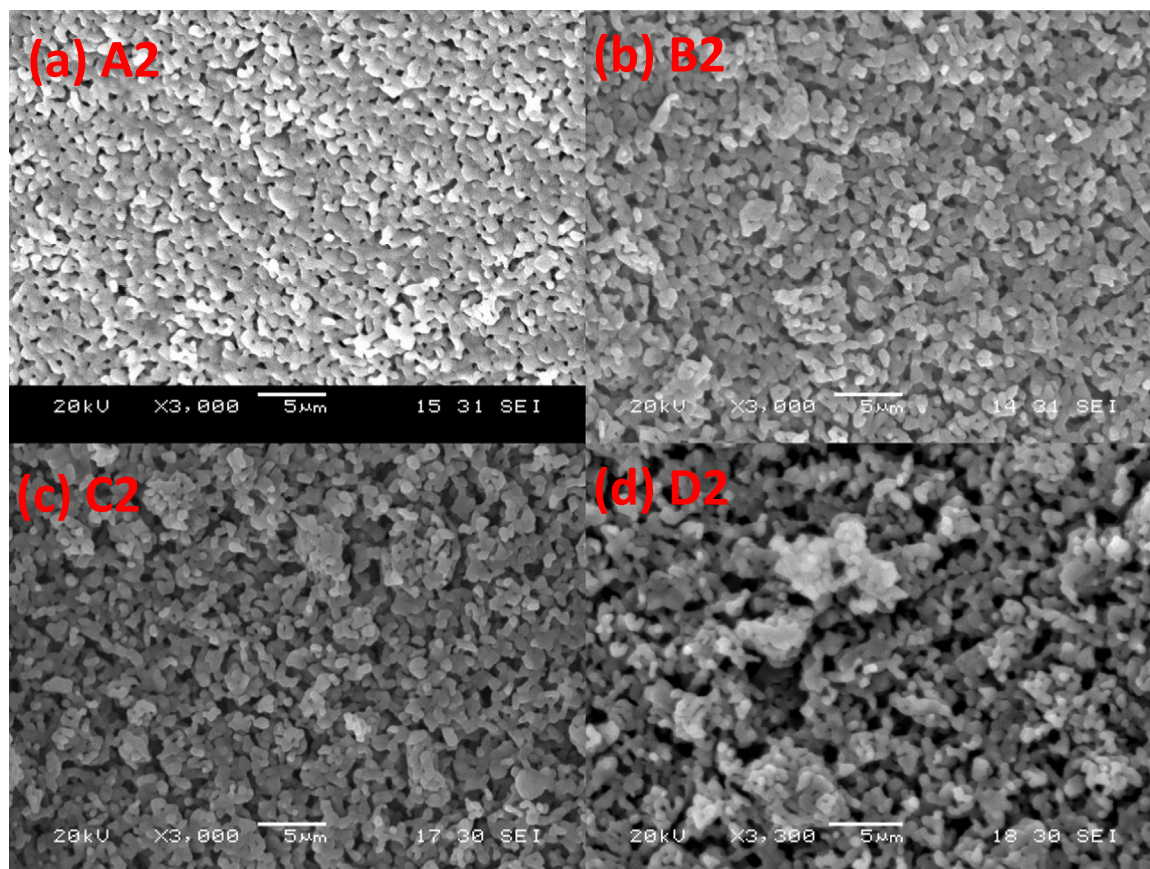


Fig. 3. SEM images of inner surfaces of samples with different polymer concentration fabricated using 15 ml min^{-1} of PVA aqueous solution as bore fluid.

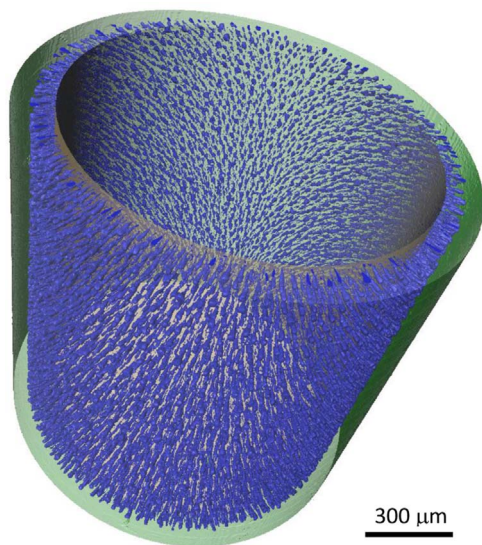


Fig. 4. 3D visualisation of the distribution of inner micro-channels in sample A2. The micro-channels are highlighted in violet and the solid layer is displayed in light green. (For interpretation of the references to color in this figure, the reader is referred to the web version of this article.)

preparation as insufficient extrusion rate of the internal coagulant could result in deformed or acentric lumen geometry. In contrast, the viscosity of PVA aqueous solution is almost three orders of magnitude higher compared with water, which leads to a much higher pressure generated from internal coagulant flow to enlarge the lumen dimension. Therefore, the fabrication process is less sensitive towards the selected extrusion rates, which makes the whole process more con-

trollable and repeatable. Fig. 2 depicts the samples fabricated from 30 wt% polymer loading. It can be observed that PVA aqueous solution with higher viscosity could effectively maintain the regularity of the morphology, with centric lumen and typical asymmetric structure. By contrast, in the counterpart prepared with water, an abnormal ‘finger-splitting’ phenomenon can be observed (Fig. 2(f)).

As suggested in previous studies [26], the mechanism of forming micro-channels could be due to the interfacial instability, such as the Rayleigh–Taylor (R–T) instability. This phenomenon occurs at the interface between two fluids with different densities and such complex processes could be affected by a number of factors, such as the mismatch in density, surface tension, viscosity and compressibility [27]. Furthermore, it is noteworthy that the final morphology can be the result of multiple instabilities: when the initial perturbation reaches a certain extent, the interactions between internal coagulant and the finger-front of micro-channels could lead to a secondary Helmholtz instability along the side of channels and subsequently the ‘finger-splitting’ phenomenon [27,28]; during which self-organized micro-channels could have amalgamation and turbulent mixing and form a highly-porous structure. As is shown in Fig. 2(g) and (h), finger-splitting can only be observed when water was used as the internal coagulant and reached a certain extrusion rate (15 ml min^{-1}), whereas the PVA aqueous solution could effectively prohibit the occurrence of such a phenomenon.

The density of the PVA aqueous solution is closer to the spinning suspension compared with water, which results in a reduced primary R–T instability. Moreover, PVA aqueous solution results in a slower solvent/non-solvent exchange rate and further inhibits momentum for non-solvent influx. Thus, the perturbation that leads to the occurrence of a secondary Helmholtz instability is also prohibited. To summarize, using PVA aqueous solution as internal coagulant could effectively standardise the pore morphology and dimension and reduce the

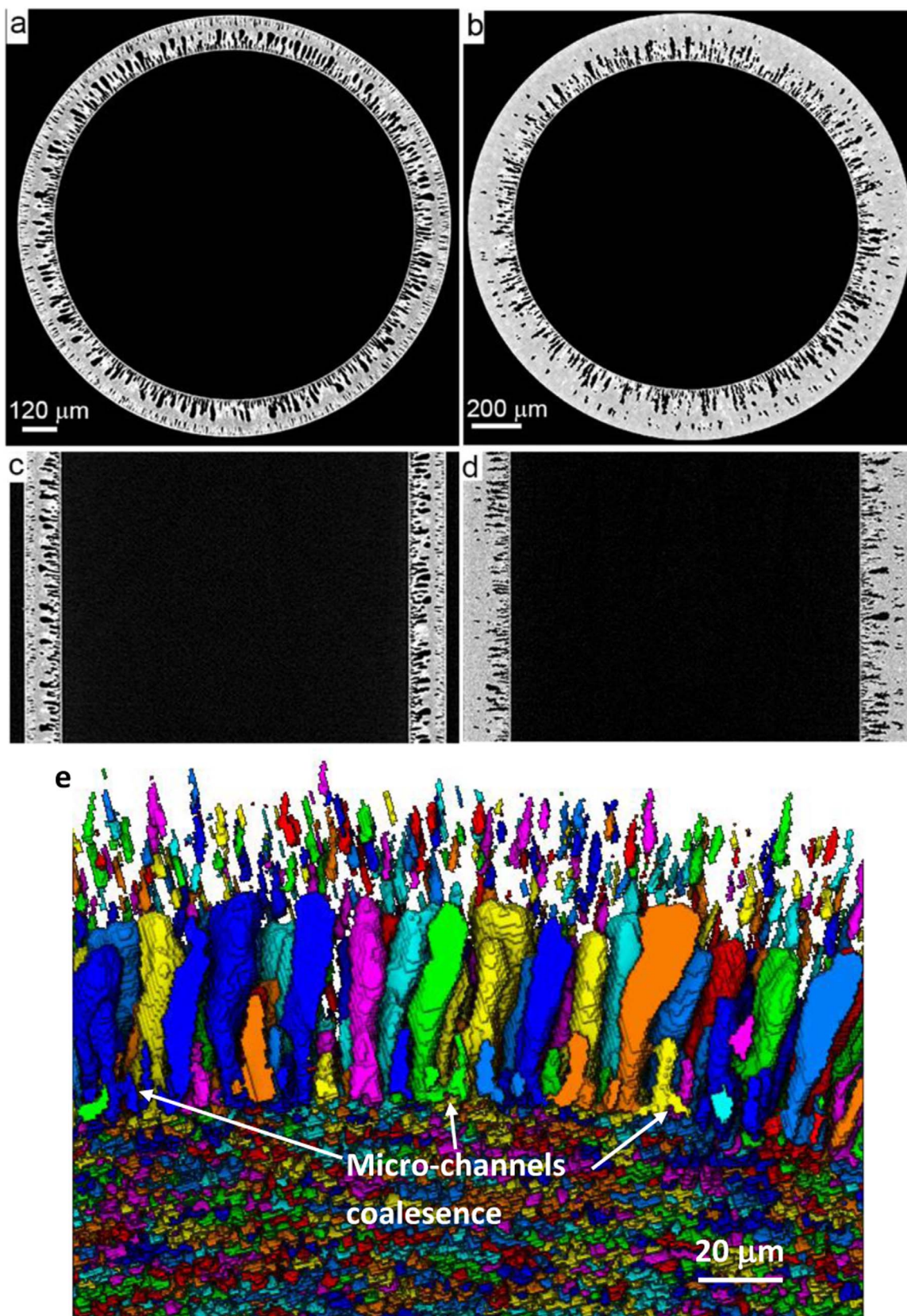


Fig. 5. The ortho slices extracted from the reconstructed volume showing the micro-structure of (a) top (c) lateral 16 wt% PVA cross sections and (b) top, (d) lateral 30 wt% PVA cross sections. (e) shows the distribution of inner and outer micro-channels. The coalescence of the micro-channels has been pointed out by white arrows.

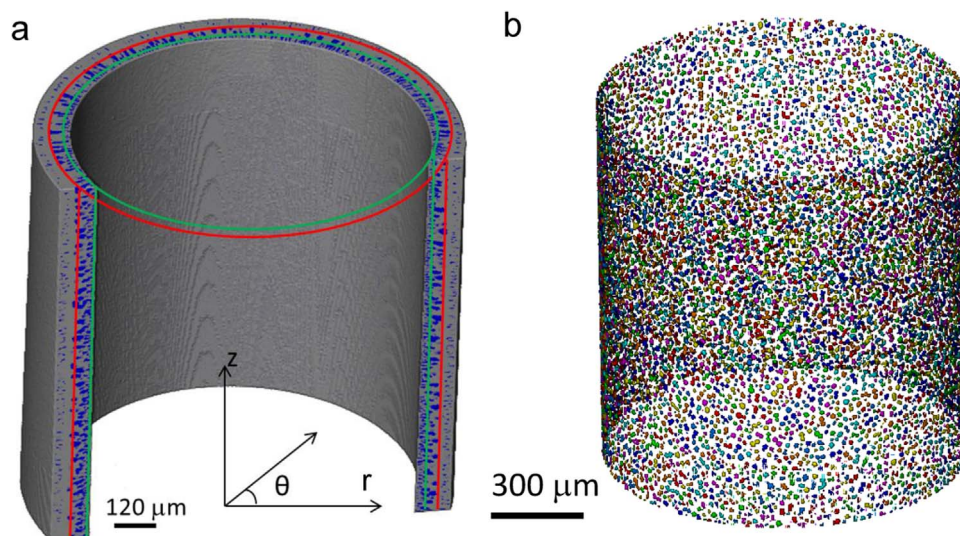


Fig. 6. Illustration of the measurement of micro-channels. (a) Micro-channel density is measured on a series of concentric layers; (b) the intersection of the cylindrical single layer with the micro-channels. Cross-sections of each micro-channel are labelled as different colours. (For interpretation of the references to color in this figure, the reader is referred to the web version of this article.)

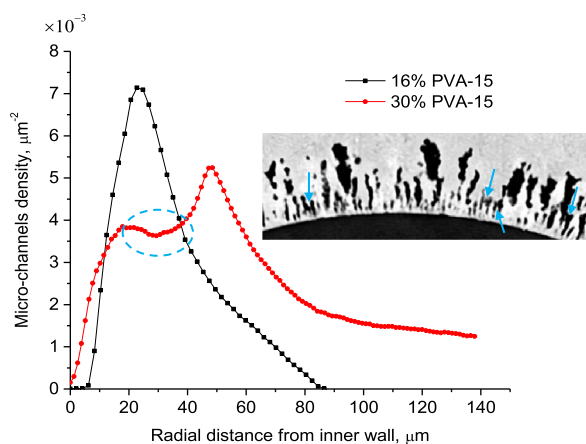


Fig. 7. Micro-channel densities as a function of radial distance for A2 (black) and D2 (red). The non-monotonic zone (marked out by dashed ellipse) is the result of the point connections between the neighbouring micro-channels, pointed out by blue arrows on the insertion of the virtual slice. (For interpretation of the references to color in this figure legend, the reader is referred to the web version of this article.)

sensitivity towards the variation of extrusion rates, which is of considerable interest in terms of large-scale manufacturing.

3.1.2. The sponge-like layer

Fig. 3 displays higher magnification SEM images of the spongy inner surfaces of samples with different polymer binder loading. It can be observed that packing of particles becomes less dense as the polymer concentration increases, which is due to the effects on precipitate rate. The pore size on the inner surface normally denotes the entrance sizes of micro-channels. The entrance shrinks during the phase inversion process as the suspension surrounding the entrance precipitates. Therefore, low polymer concentration prolongs the precipitation process and leads to further shrinkage of channel entrances to a smaller dimension, which is in good agreement with the previous study [29].

3.2. Characterization of micro-channels using X-ray CT

The reconstructed volume from the CT scan can be visualized in 3D, e.g. Sample D2 shown in Fig. 4. The distribution of the micro-channels is highlighted in blue in the transparent cross-section (green). The top

and lateral slices extracted from the reconstructed volumes of A2 and D2 samples are shown in Fig. 5. It can be seen that the micro-channels in samples from 16 wt% polymer loading appear to have a teardrop shape, whereas the micro-channels in 30 wt% PVA sample are thinner and elongated with rough edges, which is due to increased density/viscosity from higher polymer concentration and consequently reduced momentum for micro-channel growth. Moreover, both samples show two types of micro-channels: inner micro-channels connect to the inner surface of the tube and outer micro-channels at the outer layer of the tube. The inner micro-channels is subjected to the internal coagulant adjustment and are investigated in this study. The morphology of the micro-channels is shown in Fig. 5(e), taking A2 as an example. Each individual micro-channels is labelled as a different colour. Accordingly it is straightforward to spot the coalescence of the neighbouring micro-channels which are shown as the same colour and indicated by the white arrows.

It is the first time known to the authors, that the diameter and density of the micro-channels have been characterized based on 3D reconstruction of the hollow fiber. The quantifications are based on the following algorithm: 1) a polar coordinates system was defined for the hollow fiber, and the origin of the system was the mass centre of the fiber (Fig. 6a); 2) a series of 1 voxel-thick concentric layers were defined along the radial direction (r) at the step size of 1 voxel, shown as the green and red lines in Fig. 6(a); 3) the intersection of the concentric layers and the micro-channels were extracted and labelled in different colours individually (Fig. 6b). The radial range of the concentric layers are selected so that only inner micro-channels are measured in this study; 4) the micro-channel density was calculated by dividing the number of the micro-channels over the area of the circular layer for each radial distance. Similarly, the diameter of the micro-channels can be measured at each concentric layer.

3.2.1. Micro-channel density

For applications like waste water treatment or gas separation, the density of micro-channels may not be the critical factor as separation performance is mainly determined by the properties of the separation layer (the sponge-like layer). However, for applications such as membrane reactors, distributors and catalytic converters, each micro-channel functions as a micro-reactor. Therefore, the micro-channel density is the major factor that influences the reaction kinetics and reactor performance. By comparing the variation of the micro-channel densities with the polymer concentrations, better control of the

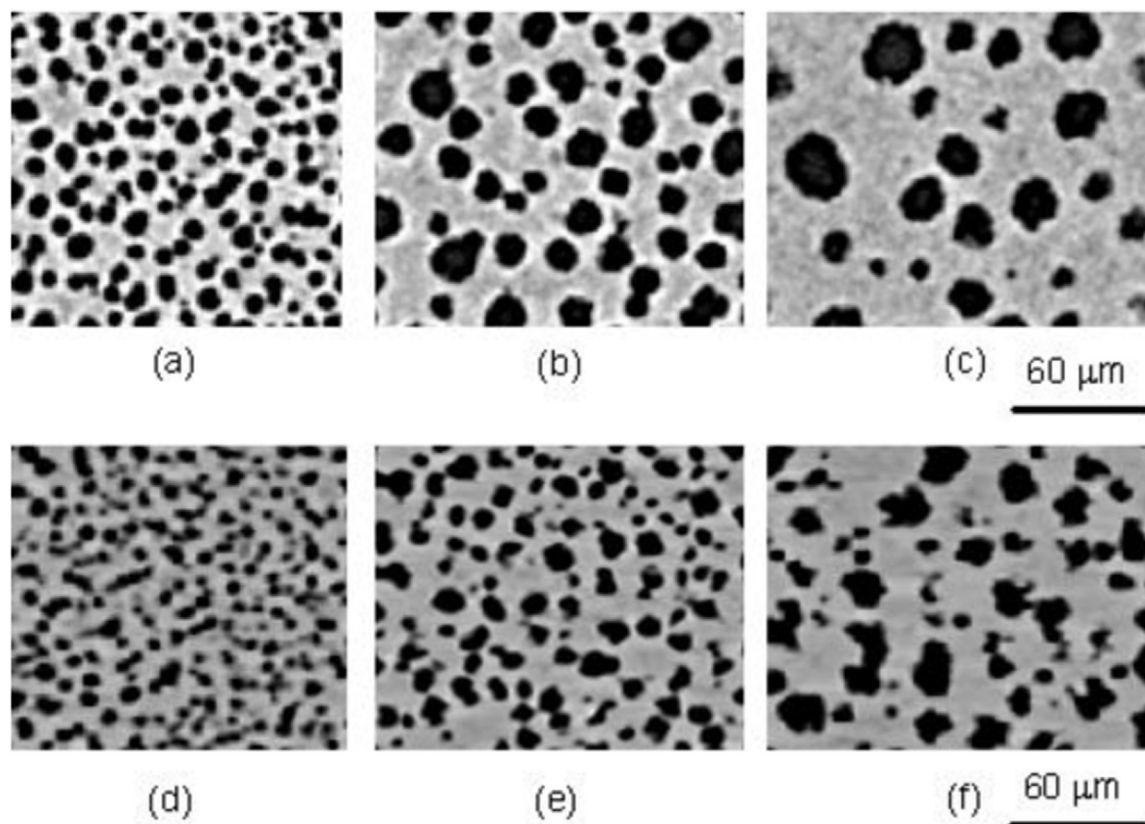


Fig. 8. X-ray CT virtual slices showing the cross-sections of the micro-channels in the radial direction at 20, 40 and 60 μm from inner wall for (a)–(c) A2 and (d)–(f) D2 respectively.

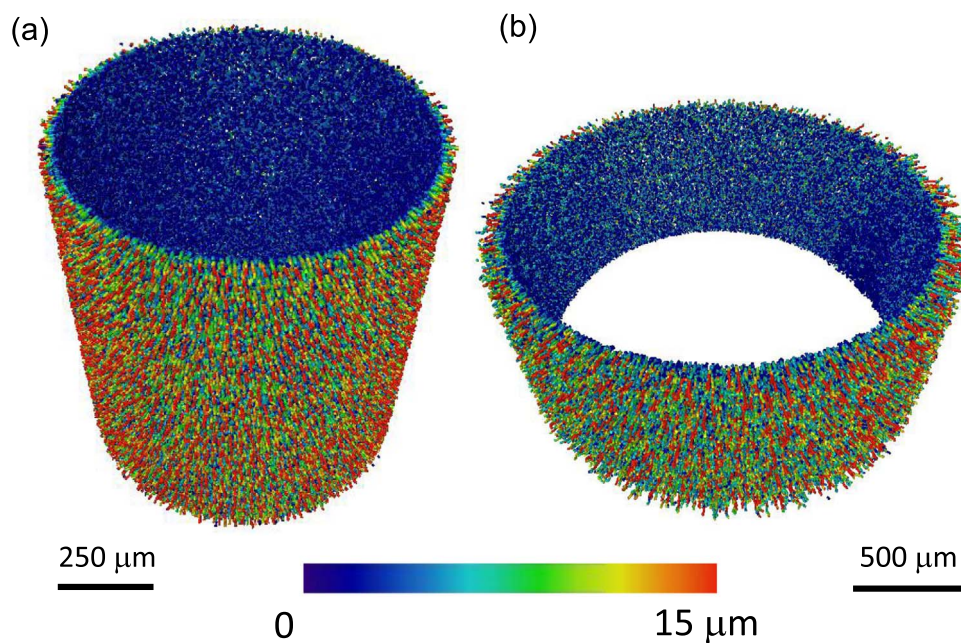


Fig. 9. 3D distribution of the colour-coded diameter of the micro-channels for (a) A2 and (b) D2 samples. (For interpretation of the references to color in this figure legend, the reader is referred to the web version of this article.)

microstructure can be achieved during the fabrication process, so as to improve the performance in membrane reactor applications. The micro-channel density as a function of radial distance from the inner wall is plotted in Fig. 7. The origin indicates that the measurement starts from the inner wall of the fiber. The peak channel density of sample A2 ($7.2 \times 10^{-3} \mu\text{m}^{-2}$) is approximately 40% higher compared with the 30 wt% counterpart (Sample D2, $5.2 \times 10^{-3} \mu\text{m}^{-2}$), which is due to reduced momentum from higher polymer concentration. This

phenomenon is in good agreement with the previous study [26].

The density is supposed to be highest at the inner wall and decrease along the radial direction. However, it increases first and then decreases with radial distance for both samples. This phenomenon is possibly a joint result from two facts: 1) the resolution is lower (i.e. $1.03 \mu\text{m}$) than the smallest micro-pore size (about $0.5 \mu\text{m}$) at the inner wall, where an inner skin layer is normally formed at the interface between solvent/non-solvent. Therefore, some of the smallest micro-

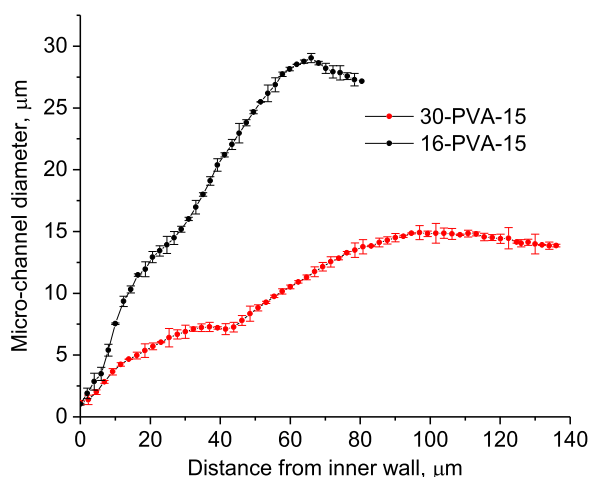


Fig. 10. Diameter of the micro-channels plotted against the radial distance for A2 (16-PVA-15) and D2 (30-PVA-15) samples.

Table 2

Dimension, pure water flux and mean flow pore size of various samples.

Sample No.	Water flux ($\text{L m}^{-2} \text{h}^{-1} \text{bar}^{-1}$)	Sponge pore ($\pm 10 \text{ nm}$)
A1	1710 ± 34	308
A2	2486 ± 70	288
B1	3661 ± 63	383
B2	4043 ± 46	384
C1	4672 ± 10	397
C2	4722 ± 19	395
D1	5049 ± 65	416
D2	5183 ± 53	422

scopic channels were not resolved within approximately $10 \mu\text{m}$ from inner wall; 2) neighbouring micro-channels are prone to merge in the vicinity of the initiation point. As the distance increases from the inner wall, they will split, resulting in an increasing micro-channel density until reaching a peak value. It is noted that the plot of D2 exhibits a non-monotonic trend from 20 to $40 \mu\text{m}$ distance, as indicated by the dashed circle in Fig. 7. This results from the coalescence of the neighbouring micro-channels, (pointed out by the blue arrows on the insertion). The coalescence occurs at the end of the tiny micro-channels due to the circumferential growth. These short micro-channels disappear beyond this point and only larger micro-channels can be seen, resulting in a decrease of the micro-channels density. The hierarchical order of the micro-channels is clearly described in the literature [26].

3.2.2. Dimension of the micro-channels

For liquid/gas separation applications, the dimension of micro-channels has negligible effects on transport properties, as the intergranular pore size of the separation layer (sponge region) determines the transport mechanisms and permeability [1]. However, for membrane reactor applications, in which the loading and distribution of catalysts play an essential role, the dimension of micro-channels considerably influences catalyst incorporation and subsequently the catalytic activity [30,31]. The cross-sections of the micro-channels at different distances away from the inner wall are shown in Fig. 8. It is observed that sample A2 shows a larger, more circular morphology compared with that in Sample D2 and the diameter increases for both types of samples. The colour-coded diameter distributions are visualized in 3D for both samples (Fig. 9): it is found that the overall size of the micro-channels is larger for A2. The trend of the micro-channels variation is compared and quantified by plotting diameter vs. radial distance for both samples (Fig. 10): 1) as the polymer loading increases, the average micro-channel diameter is dramatically reduced (A2 has a channel diameter twice as large as D2, with a maximum

channel diameter of 29 and $15 \mu\text{m}$ for A2 and D2, respectively); 2) higher polymer loading (D2) leads to four times lower growth rate of the micro-channels diameter; 3) higher polymer loading (D2) results in 60% longer micro-channels in radial direction.

3.3. Mean flow pore size and pure water flux

Mass transport properties of the hollow fiber are critical in the application of gas separation and electrodes for tubular SOFCs. It is meaningful to inspect the relation between the mass transport and the porous phase in this material. In this study, the mean flow pore size was measured by the bubble point method and the results are shown in Table 2. Results show that the polymer concentration in the suspension has a marked influence in the size of inter-granule packing pores of the separation layer, showing a directly proportional relationship. As the polymer loading is enhanced from 16 wt% to 30 wt%, the mean flow pore size increases from $280 \mu\text{m}$ to more than $400 \mu\text{m}$. The pure water flux was measured using a dead-end test rig and the results are displayed in Table 2. Pure water flux displays a directly proportional relationship with polymer concentration, which is in good agreement with mean flow pore size. As the polymer concentration increases from 16 wt% to 30 wt%, the mean flow pore size of separation layer increases by approximately 50%, whereas the pure water flux more than doubles. Despite the larger size of the micro-channels, and the higher micro-channel density of 16 wt% samples (A1 and A2), the lower water flux proves that the mass transport property is mainly controlled by the pore size in the sponge region. This also indicates that the existence of micro-channels could effectively facilitate mass transport with negligible resistance.

4. Conclusion

A series of alumina hollow fibers have been fabricated with varied concentration of the polymer binder and a novel polymer-based internal coagulant demonstrating that PVA aqueous solution could be a promising replacement for water, which has been extensively used. The resultant fibers have dramatically improved uniformity as well as better repeatability between different batches as the preparation procedure becomes less sensitive towards corresponding extrusion rates. Moreover, irregular lumen geometries and undesirable finger splitting phenomena could be effectively inhibited.

For the first time, X-ray CT has been applied to provide 3D structural reconstruction and characterization in terms of micro-channel density and dimensions. 30% polymer concentration of the polymer binder results in 60% more elongated and rough micro-channels with 50% lower diameter ($15 \mu\text{m}$) compared to the sample of 16% polymer concentration ($29 \mu\text{m}$) and lower density close to the inner wall (micro-channel density decreased by 40%). However, the mass transport (water permeation) is superior in the samples of 30% polymer binder concentration due to a larger pore size in the sponge region (approximately 420 nm compared to 280 nm for 16% polymer concentration), suggesting that mass transport properties mainly depend on separation layer and micro-channels may not introduce additional resistance. Such insight into actual 3D micro-structure could provide a better insight into the phase inversion process and help to realize practical structural design and tailoring for various applications.

Acknowledgements

The authors acknowledge support from the EPSRC under grants EP/N032888/1 and EP/M014045/1, PRS acknowledges funding from the Royal Academy of Engineering.

Appendix A. Supplementary material

Supplementary data associated with this article can be found in the online version at doi:10.1016/j.memsci.2017.01.004.

References

- [1] K. Li, Ceramic Membranes for Separation and Reaction, John Wiley & Sons Ltd, Chichester, UK, 2007.
- [2] S.M. Jamil, et al., Recent fabrication techniques for micro-tubular solid oxide fuel cell support: a review, *J. Eur. Ceram. Soc.* 35 (1) (2015) 1–22.
- [3] T. Li, Z. Wu, K. Li, Co-extrusion of electrolyte/anode functional layer/anode triple-layer ceramic hollow fibres for micro-tubular solid oxide fuel cells—electrochemical performance study, *J. Power Sources* 273 (2015) 999–1005.
- [4] H. Strathmann, K. Kock, The formation mechanism of phase inversion membranes, *Desalination* 21 (3) (1977) 241–255.
- [5] S. Liu, Preparation of porous aluminium oxide (Al₂O₃) hollow fibre membranes by a combined phase-inversion and sintering method, *Ceram. Int.* 29 (8) (2003) 875–881.
- [6] X. Meng, et al., Microstructure tailoring of YSZ/Ni-YSZ dual-layer hollow fibers for micro-tubular solid oxide fuel cell application, *Int. J. Hydrog. Energy* 38 (16) (2013) 6780–6788.
- [7] C. Ren, et al., Effect of casting slurry composition on anode support microstructure and cell performance of MT-SOFCs by phase inversion method, *Electrochim. Acta* 149 (2014) 159–166.
- [8] C. Ren, et al., Effect of PEG additive on anode microstructure and cell performance of anode-supported MT-SOFCs fabricated by phase inversion method, *J. Power Sources* 279 (2015) 774–780.
- [9] C. Ren, et al., Fabrication of micro-tubular solid oxide fuel cells using sulfur-free polymer binder via a phase inversion method, *J. Power Sources* 290 (2015) 1–7.
- [10] Shaomin Liu, et al., Preparation and characterisation of SrCe_{0.95}Yb_{0.05}O_{2.975} hollow fibre membranes, *J. Membr. Sci.* 193 (2) (2001) 249–260.
- [11] Xiaoyao Tan, Shaomin Liu, K. Li, Preparation and characterization of inorganic hollow fiber membranes, *J. Membr. Sci.* 188 (1) (2001) 87–95.
- [12] Y.-c. Karen Chen-Wiegart, et al., 3D Non-destructive morphological analysis of a solid oxide fuel cell anode using full-field X-ray nano-tomography, *J. Power Sources* 218 (2012) 348–351.
- [13] J. Viguié, et al., Characterisation of 3D porous macrostructure of hollow fibre membranes using X-ray tomography—effects of some spinning process conditions, *J. Membr. Sci.* 435 (2013) 11–20.
- [14] S. Dai, et al., Characterization of hollow fiber supported Ionic liquid membranes using microfocus X-ray computed tomography, *J. Membr. Sci.* 492 (2015) 497–504.
- [15] D. Kennouche, et al., Combined electrochemical and X-ray tomography study of the high temperature evolution of Nickel – Yttria Stabilized Zirconia solid oxide fuel cell anodes, *J. Power Sources* 307 (2016) 604–612.
- [16] M. Andisheh-Tadbir, F.P. Orfino, E. Kjeang, Three-dimensional phase segregation of micro-porous layers for fuel cells by nano-scale X-ray computed tomography, *J. Power Sources* 310 (2016) 61–69.
- [17] P. Trogadas, et al., X-ray micro-tomography as a diagnostic tool for the electrode degradation in vanadium redox flow batteries, *Electrochem. Commun.* 48 (2014) 155–159.
- [18] U. Doraswami, et al., Modelling the effects of measured anode triple-phase boundary densities on the performance of micro-tubular hollow fiber SOFCs, *Solid State Ion.* 192 (1) (2011) 494–500.
- [19] S.S. Manickam, J.R. McCutcheon, Characterization of polymeric nonwovens using porosimetry, porometry and X-ray computed tomography, *J. Membr. Sci.* 407–408 (2012) 108–115.
- [20] R. Schurch, et al., Comparison and combination of imaging techniques for three dimensional analysis of electrical trees, *IEEE Trans. Dielectr. Electr. Insul.* 22 (2) (2015) 709–719.
- [21] Y. Sagara, et al., Abdominal CT: comparison of low-dose CT With adaptive statistical iterative reconstruction and routine-dose CT With filtered back projection in 53 patients, *Am. J. Roentgenol.* 195 (3) (2010) 713–719.
- [22] G. Lauritsch, W.H. Haerer, Theoretical framework for filtered back projection in tomosynthesis, *Med. Imaging'98: Int. Soc. Opt. Photonics* 3338 (1998) 1127–1137.
- [23] S. Stock, X-ray microtomography of materials, *Int. Mater. Rev.* 44 (4) (1999) 141–164.
- [24] S. Stock, Recent advances in X-ray microtomography applied to materials, *Int. Mater. Rev.* 53 (3) (2008) 129–181.
- [25] E. Maire, P. Withers, Quantitative X-ray tomography, *Int. Mater. Rev.* 59 (1) (2014) 1–43.
- [26] M. Lee, et al., Formation of micro-channels in ceramic membranes – spatial structure, simulation, and potential use in water treatment, *J. Membr. Sci.* 483 (2015) 1–14.
- [27] D.H. Sharp, An overview of rayleigh-taylor instability, *Phys. D* 12 (1–3) (1984) 3–10.
- [28] B. Wang, Z. Lai, Finger-like voids induced by viscous fingering during phase inversion of alumina/PES/NMP suspensions, *J. Membr. Sci.* 405–406 (2012) 275–283.
- [29] M. Lee, et al., Micro-structured alumina multi-channel capillary tubes and monoliths, *J. Membr. Sci.* 489 (2015) 64–72.
- [30] A. Gouveia Gil, et al., A catalytic hollow fibre membrane reactor for combined steam methane reforming and water gas shift reaction, *Chem. Eng. Sci.* 137 (2015) 364–372.
- [31] N.H. Othman, Z. Wu, K. Li, A micro-structured La_{0.6}Sr_{0.4}Co_{0.2}Fe_{0.8}O_{3–δ} hollow fibre membrane reactor for oxidative coupling of methane, *J. Membr. Sci.* 468 (2014) 31–41.